HEALTH AND MEDICINE

4D physiologically adaptable cardiac patch: A 4-month in vivo study for the treatment of myocardial infarction

Haitao Cui[1], Chengyu Liu[2], Timothy Esworthy[1], Yimin Huang[2], Zu-xi Yu[2], Xuan Zhou[1], Hong San[2], Se-jun Lee[1], Sung Yun Hann[1], Manfred Boehm[2], Muhammad Mohiuddin[3], John P. Fisher[4], Lijie Grace Zhang[1,5,6,7]*

There has been considerable progress in engineering cardiac scaffolds for the treatment of myocardial infarction (MI). However, it is still challenging to replicate the structural specificity and variability of cardiac tissues using traditional bioengineering approaches. In this study, a four-dimensional (4D) cardiac patch with physiological adaptability has been printed by beam-scanning stereolithography. By combining a unique 4D self-morphing capacity with expandable microstructure, the specific design has been shown to improve both the biomechanical properties of the patches themselves and the dynamic integration of the patch with the beating heart. Our results demonstrate improved vascularization and cardiomyocyte maturation in vitro under physiologically relevant mechanical stimulation, as well as increased cell engraftment and vascular supply in a murine chronic MI model. This work not only potentially provides an effective treatment method for MI but also contributes a cutting-edge methodology to enhance the structural design of complex tissues for organ regeneration.

INTRODUCTION

Cardiovascular disease associated with myocardial infarction (MI) is a major cause of morbidity and mortality worldwide (*1*, *2*). The heart is composed of dynamic and multicellular tissues that exhibit highly specific structural and functional characteristics. Adult cardiac muscle is thought to lack the ability to self-repair and regenerate after MI. Traditional cardiac patches serve as temporary mechanical supporting systems to prevent the progression of postinfarction left ventricular (LV) remodeling (*2*). However, the damaged myocardium is still unable to self-restore, and the subsequent maladaptive remodeling is typically irreversible (*2*). Because of the shortage of organ donors and the limited retention of cellular therapies, the field of cardiac engineering has emerged to generate functional cardiac tissues to provide a promising alternative means to repair damaged heart tissue (*3*, *4*). In addition to playing a role in providing mechanical support, cellularized cardiac patches and scaffolds have also been investigated to restore the functionality of the damaged myocardium (*5*, *6*). Compared to synthetic materials, hydrogel-based materials derived from, or partially derived from, natural sources can mimic the specific aspects of the tissue microenvironment and can support both cell adhesion and growth (*7*). Hence, these hydrogel-based materials can provide a more favorable matrix for the growth and differentiation of cardiomyocytes (*7*, *8*). However, limitations of structural design and manufacturing techniques, as well as the low mechanical strength and weak processability of hydrogel-based patches, still make their clinical application challenging (*3*, *7*, *8*).

Because of the limited expansion and regeneration capacity of primary cardiomyocytes, the use of human induced pluripotent stem cell–derived cardiomyocytes (hiPSC-CMs) provides a continuous cell source by which to produce terminally differentiated cells and avoid controversial ethical issues in biomedical research (*9*, *10*). Although several studies have been performed with hiPSC-CMs to generate functional cardiac tissue constructs (*11*, *12*), more studies are required to explore the interaction between hiPSC-CMs and the matrix microenvironment (i.e., scaffolds and other cells) for therapeutic improvement. Hence, further studies should focus on exploring material bioactivity, architectural design and manufacturing, the biomechanical properties of tissue constructs, and the long-term in vivo development of these tissue constructs, which will ultimately affect three-dimensional (3D) cell assembly and neotissue remodeling for clinical research purposes (*2*, *10*, *13*).

In this study, a 4D hydrogel-based cardiac patch was developed with a specific smart design for physiological adaptability (or tunability) using a beam-scanning stereolithography (SL) printing technique. Beam-scanning SL printing offers an effective methodology for creating microfabricated tissue constructs with photocurable hydrogels, which are able to achieve many essential requirements in manufacturing tissue micropatterns and macroarchitectures (*14*). The printing speed and laser intensity are able to be varied as required, which provides the ability to tailor the cross-linking degree of the inks and, therefore, affects the physicochemical properties of hydrogels. Moreover, it was observed that a light-induced graded internal stress, followed by a solvent-induced relaxation of material, drove an autonomous 4D morphing of the objects after printing (*15*, *16*). It was found that this self-morphing process was able to achieve conformations that were nearly identical to the surface curvature of the heart. Moreover, taking the physiological features of the cardiac tissue and the physical properties of the hydrogel into account, a highly stretchable microstructure was created to allow for an easy switch of fiber arrangement from a wavy pattern to a mesh pattern, in accordance with the diastole and systole in the cardiac cycle. The specific design was expected to increase the mechanical tolerance of the printed hydrogel and to decrease the unfavorable effect of hiPSC-CM residence on the printed patches when exposed to the dynamic mechanics. By triculturing cardiomyocytes,

---

[1]Department of Mechanical and Aerospace Engineering, The George Washington University, Washington, DC 20052, USA. [2]National Heart, Lung, and Blood Institute, National Institutes of Health, Bethesda, MD 20892, USA. [3]Cardiac Xenotransplantation Program, Department of Surgery, University of Maryland, Baltimore, MD 21201, USA. [4]Fischell Department of Bioengineering, University of Maryland, College Park, MD 20742, USA. [5]Department of Electrical and Computer Engineering, The George Washington University, Washington, DC 20052, USA. [6]Department of Biomedical Engineering, The George Washington University, Washington, DC 20052, USA. [7]Department of Medicine, The George Washington University, Washington, DC 20052, USA.
*Corresponding author. Email: lgzhang@gwu.edu

mesenchymal stromal cells, and endothelial cells, the printed microfibers with specific nonlinear microstructures could reproduce the anisotropy of elastic epicardial fibers and vascular networks, which plays a crucial role in supporting the effective exchange of nutrients and metabolites, as well as guiding contracting cells for engineered cardiac tissue.

RESULTS

Design of a physiologically adaptable cardiac patch

The cardiac muscle fibers mainly consist of longitudinally bundled myofibrils (cardiomyocytes and collagen sheaths), which are surrounded by high-density capillaries (*17*, *18*). This anisotropic (directionally dependent) muscular architecture results in the coordinated electromechanical activity of the ventricles, which involves the directionally dependent myocardial contraction and the propagation of the excitation wave (*19*, *20*). As can be observed by diffusion tensor imaging (DTI) (*21*, *22*), a helical network of myofibers in the LV is organized to form a sheet structure, and the orientation of the fiber angles varies from approximately +60° to −60° across the ventricular wall (Fig. 1A). The visualization of the fiber structure illustrates the left-handed to the right-handed rotation of the fibers going from the epicardium to the endocardium in the LV (*21*). Computer-aided design (CAD)–driven 3D printing offers a promising technique by which to transform the anatomical detail of cardiac fiber maps into a highly complex arrangement of fibers within an engineered cardiac tissue (*23*). Figure 1B shows that the spiral arrangement of 3D myocardial fibers crosses the ventricular wall (a "left-handed to right-handed" spiral of the fibers going from the epicardium to the endocardium) and their 2D "mesh pattern" projections at different angles.

Moreover, another specific feature of the cardiac tissue is the diastole and systole in the cardiac cycle induced by the contraction of cardiac muscle, which generates the force for blood circulation (*8*, *24*). When taking the volume change of the heart into account, the arrangement of fibers is dynamically stretched in a selected region (Fig. 1C). Hence, the mesh pattern was changed to "hexagon or wavy pattern" in the 2D plane to adapt the change of ventricular curvature (Fig. 1D). It was able to create a highly stretchable structure with very limited deformability, which is expected to decrease the negative effect on the attached, susceptible cardiomyocytes. To mathematically characterize this design, we simplified the solid geometric model with a plane curve prototype to elaborate on the relationship between the redundant length of the stretchable structure (ΔL) and the ventricular curvature (κ) in the systole state (Fig. 1E). By the calculation, it can be estimated as

$$\Delta L = \frac{\cos^{-1}(1 - D^2\kappa^2/2)}{\kappa} - D \qquad (1)$$

where ΔL is the redundant length of the stretchable structure from straight to curve, κ is the ventricular curvature in the systole state, and D is the approximate length of fiber in the diastole state (here, $D = 400$ μm from our study). In the previous study, a light-induced 4D morphing phenomenon was demonstrated when using our customized beam-scanning SL printer (*15*, *16*). The laser-induced graded internal stress, introduced through the printing process, is a major driving force of this 4D dynamic morphing (*15*, *16*, *25*). The

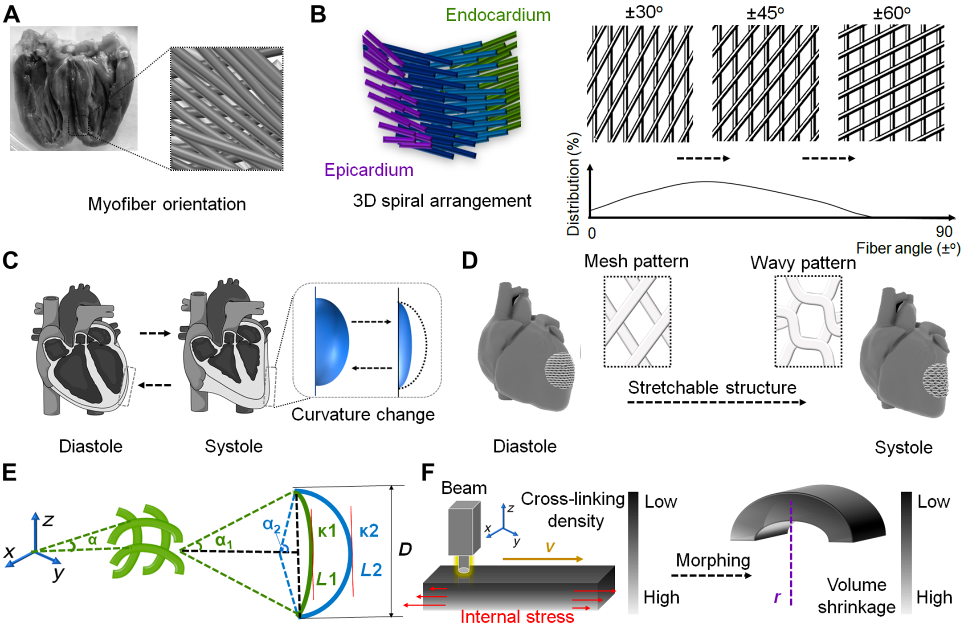

Fig. 1. Design of a physiologically adaptable cardiac patch. (**A**) Photograph of the anatomical heart and the fiber structure of the LV visualized by DTI data. (**B**) Schematic illustration of a short-sectioned LV that illustrates the variation of fiber angle from the epicardium to the endocardium. The orientation (2D mesh pattern projection) of the fiber angles varies continuously with the position across the wall and distribution changes from the apical region to the basal region. (**C**) Curvature change of cardiac tissue at two different phases (diastole and systole) of the cardiac cycle, which occurs as the heartbeat and pumping blood. (**D**) CAD design of 3D stretchable architecture on the heart. It provides dynamic stretchability without material deformation or failure when the heart repeatedly contracts and relaxes. (**E**) Representation of a simplified geometric model of the fibers in the printed object. In the selected region, the angle (α), the length of fiber (L), spatial displacement (D) and the ventricular curvature (κ) are defined with systole (*1*) and diastole (*2*) states. (**F**) Mechanism of the internal stress-induced morphing process. Uneven cross-linking density results in different volume shrinkage after stress relaxation. Photo credit: Haitao Cui, The George Washington University (GWU).

uneven cross-linking density of photocrosslinkable inks generates the difference of modulus between the upper and lower surfaces of thin objects due to laser energy attenuation, leading to different volume shrinkage after stress relaxation (*15*). However, when multilayers were printed, the beam-scanning SL printing resulted in the repeated cross-linking of previous layers. The bottom layers had a higher cross-linking density. In this case, the bottom layer, which was cured the earliest, adhered to the substrate and could not shrink freely, while the top layer during printing could gradually and spontaneously shrink because of the release of internal stress. Thus, the printed objects have a tendency to bend toward the newly cured layer. We also found the humidity-responsive, reversible 4D phenomenon, which is swelling-induced stretching and dehydration-induced bending (*15*). After printing, the printed patch can transform from a 3D flat pattern to the 4D curved architecture when appropriate printing parameters are selected (Fig. 1F), which will be elaborated upon in the next section. It was hypothesized that by integrating a unique 4D self-morphing ability within the construct, the structural expandability of the design would improve the physiological adaptability of the engineered cardiac patch to the heart for in vivo cardiac regeneration.

Printing and optimization of the cardiac patch

A gelatin-based printable ink consisting of gelatin methacrylate (GelMA) and polyethylene glycol diacrylate (PEGDA) was used to create the anisotropic cardiac patch with myocardial fiber orientation. As a chemical derivative of gelatin [gelatin is derived from the hydrolysis of collagen, which is a major component of the extracellular matrix (ECM)], GelMA is a photocurable biomaterial with many arginine-glycine-aspartic acids and other peptide sequences that can significantly promote cell attachment and proliferation (*14*). The PEGDA solution was mixed with GelMA to decrease the swelling volume and to increase the mechanical modulus and structural stability of the printed hydrogels. The structural characteristics and mechanical properties of the printed hydrogels were determined by fiber design, printing parameters, the ink concentration, and mixing ratio of GelMA and PEGDA. To optimize the fiber design, stacked wavy architectures were generated with fiber width of 100, 200, and 400 μm, fill density of 20, 40, and 60%, and fiber angles (θ) of 30°, 45°, and 60° between each layer with two, four, and eight layers, respectively, using 10% GelMA and 10% PEGDA. The laser intensity, working distance, ink volume, and temperature were set to the same conditions as our previous studies (*15*, *26*, *27*) to eliminate the effect of the printing parameters. In this situation, the printing speed of the laser-based SL printing affects the photocuring performance, the structural accuracy (fineness), and the curvature of the 4D self-morphing. To ensure the complete solidification of the inks, a printing speed of ≤10 mm/s was set on the basis of our previous trials. By varying the printing speed (cross-linking density), a series of 4D self-morphing patches (wave pattern) were obtained with different curvatures. The mesh-patterned patches also exhibited a similar 4D morphing behavior. In all 4D self-morphing structures, the degree of deformation largely depends on the swelling, water content, and ionic strength. After 4D morphing, the wave-patterned patches maintained their wavy structure with a slight deformation. In our study, the bending of macrostructure does not significantly affect the microstructure. Figure 2A shows the curvature change of 4D morphing with increasing printing speed. Similar to the 4D morphing mathematical model by stress relaxation in the previous study (*15*), the relationship between the 4D curvature and printing speed can be modeled with the materials and printing parameters using the following equation

$$1/r = 4.78\frac{\chi_0}{2.53 - \ln \nu}\left[\mathrm{mm}^{-1}\right] \tag{2}$$

where r is the radius of the object curvature after 4D morphing, ν is the printing speed (millimeters per second), and χ_0 is the shrinkage, which is dependent on both the material and the immersion medium. Here, $\chi_0 = 0.012\ \mathrm{s}^{-1}$ in aqueous solution. The results demonstrated that the patches printed with a print speed (6 mm/s) had an appropriate curvature with the 4D morphing to obtain a sufficient integration with the LV surface of the mouse hearts.

As is shown in Fig. 2B, the printing accuracy of different fiber width, fiber angle, layer number, and fill density of the fiber arrangement was investigated. The fiber pattern with a 100-μm width showed significantly lower accuracy (≈50%) when compared to both fibers with 200-μm (>70%) and 400-μm (>90%) widths. In addition, the fiber pattern with a 60% fill density showed lower accuracy than the fiber pattern with 40% fill density. This implies that the fiber pattern with higher fill density or lower width is associated with more directional changes of the laser head per unit area, which is a function of the limitation of the printing resolution. In addition, there was no significant difference in the accuracy observed when increasing the number of stacked fibers (or fiber angles) due to the high reproducibility of the SL printing (fig. S1A). It was observed that smaller fiber widths or higher fill densities had a higher surface area per unit area, which was beneficial for the attachment of more cells, as the increased surface area better mimics the native myofibers. According to a previous study, the quantitative measurement of fiber angles showed that the dominant distribution of fiber angle was +45° to −45° from the epicardium to the endocardium (*21*). Therefore, a fiber pattern was printed with a 200-μm width, 40% fill density, and a maximum angle of 45° for adjacent layers to optimize the mechanical properties of the hydrogel patches.

To test and measure the mechanical (both compression and tensile) modulus of the hydrogels, we varied the mixed weight ratio of GelMA and PEGDA from 5 to 20% (Fig. 2C and fig. S1, B and C). The results demonstrated that the mechanical moduli of the hydrogels fall within the range of the native myocardium modulus (≈10^1 to 10^2 kPa) in the physiological strain regime (*28*, *29*). In addition, swelling testing showed that when GelMA was mixed with PEGDA, the printed hydrogels maintained excellent structural stability without notable swelling (fig. S1D). With consideration for the optimized ink viscosity and hydrogel elasticity, the inks used to fabricate our myofiber patches were formulated with concentrations of 5% GelMA and PEGDA (5, 10, and 15%) and were effectively printed on the basis of our design. Figure 2D shows the optical and 3D surface plot images of the patches printed by 5% GelMA and 15% PEGDA with a 200-μm width, 40% fill density, and a 45° angle for adjacent layers. The fluorescent images of the 3D printed patches are also displayed (fig. S2A). The anisotropic behaviors of the wavy-patterned patches in the horizontal (x) and the vertical (y) direction demonstrated that uniaxial tension on the fiber pattern resulted in different deformation and stress generation in a directionally dependent manner (Fig. 2E). In particular, the stress-strain curve of the patch with 5% GelMA and 15% PEGDA was consistent with the tensile features of the native myocardium within the physiological strain regime (Fig. 2F) (*19*, *30*). The fatigue was obvious along the y direction at the initial

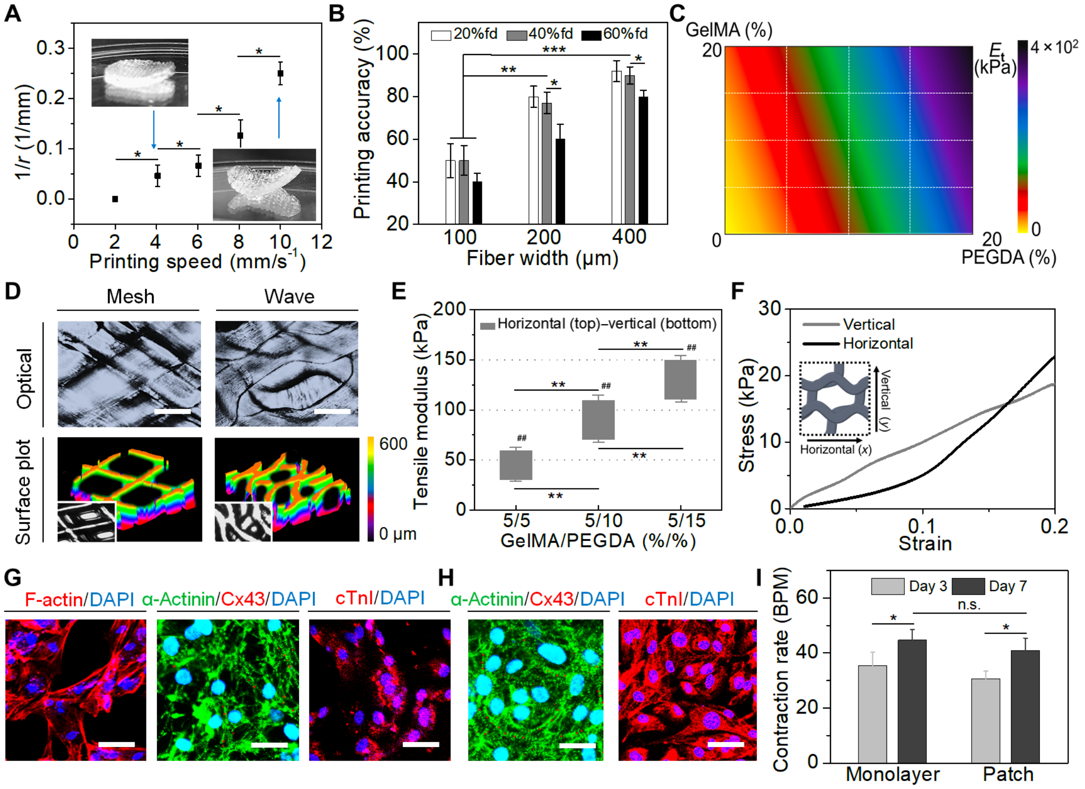

Fig. 2. Printing of smart cardiac patch and optimization. (**A**) Curvature change of 4D morphing versus printing speed (means ± SD, $n \geq 6$, $^*P < 0.05$). (**B**) Printing accuracy of the hydrogel patches versus fiber width for different fill density (fd; means ± SD, $n \geq 6$, $^*P < 0.05$, $^{**}P < 0.01$, and $^{***}P < 0.001$). (**C**) Color map of tensile moduli of the patches with varying GelMA and PEGDA concentrations. (**D**) Optical and 3D surface plot images of the patches. Scale bars, 200 μm. (**E**) Average elasticity values of the wave-patterned patches in horizontal (*x*) and vertical (*y*) directions. Number sign (#) shows the statistical comparison between the horizontal and vertical directions (means ± SD, $n \geq 6$, $^{**}P < 0.01$ and $^{\#\#}P < 0.01$). (**F**) Uniaxial tensile stress-strain curves of 5% GelMA and 15% PEGDA. Immunostaining of cell morphology (F-actin; red), sarcomeric structure (α-actinin; green), gap junction [connexin 43 (Cx43); red], and contractile protein [cardiac troponin I (cTnI); red] on the patches on (**G**) day 1 and (**H**) day 7. Scale bars, 20 μm. (**I**) Beating rate of hiPSC-CMs on the patch and well plate on day 3 and day 7 (means ± SD, $n \geq 6$, $^*P < 0.05$; n.s. no significant difference). BPM, beats per minute. Photo credit: Haitao Cui, GWU.

stage, which is attributed to the lower connectivity of fibers in the *y* direction and higher extendibility of the wavy-patterned fibers in the *x* direction. It is expected that this "physiologically adaptable" design would increase the stretchability and stability of the hydrogel patches, allowing them to absorb and release energy against the force of cardiac contraction (*31*, *32*). Compared to the mesh design, the current architecture would allow for structural compliance of the hydrogel fibers without notable deformation. Moreover, the successfully printed patterns also well represent the microstructure of the native myocardial tissue, which is formed from collagen fibers and other ECM proteins, together with cardiomyocytes. However, the width of the myofibers within the myocardial tissue was much smaller (≈30 to 40 μm) than the printed pattern (≈200 μm), which is largely a limitation of the resolution of the currently available technology.

In vitro characterization of cardiac patches

After the optimization of both the printing parameters and the ink formulation, the cardiac patches were manufactured with 5% GelMA and 15% PEGDA using a beam-scanning SL printing system. The wavy-patterned patches with a diameter of 8 mm and a thickness of 600 μm were used to perform the in vitro studies, while the mesh-patterned patches of the same fiber volume fraction served as the control. By keeping the same surface area across the different construct patterns, we could ensure that there would be the same available cell number for each of the patches. Upon analysis, the redundant length (ΔL) of the stretchable structure was determined to be around 140 μm. Because of their capacity for restoring cardiac function in previous studies, hiPSC-CMs were cultured using the same protocol developed at the National Heart, Lung, and Blood Institute (NHLBI) (*33*). Before cell seeding, a thin layer of Matrigel was precoated on the well plate or patches' surface to improve the hiPSC-CM adhesion. By day 7, spontaneous contractions of monolayer hiPSC-CMs were observed (fig. S2B and movie S1), and immunostaining results demonstrated that hiPSC-CMs displayed specific myocardial protein expression, including sarcomeric alpha-actinin (α-actinin), connexin 43 (Cx43), and cardiac troponin I (cTnI). (fig. S2, C and D). The cell-laden ink was printed by mixing 1×10^6 per ml of hiPSC-CMs with 5% GelMA and 15% PEGDA. However, a decrease in the metabolic activity of the hiPSC-CMs was observed, and the distinct cardiac beating behavior was not evident (fig. S2, E and F). These observations were likely the result of the limited 3D space within the hydrogel. Hence, a postseeding approach was then applied to fabricate the cardiac patches. Compared to the cell-laden samples, the hiPSC-CMs seeded on the patches showed significantly higher proliferation and beating rate. The attached hiPSC-CMs exhibited spontaneous contractions along the fibers on day 3 (movie S2). Moreover, the immunostaining images revealed robust F-actin, α-actinin, Cx43, and cTnI expression of hiPSC-CMs on the printed patches (Fig. 2G). After 7 days of culture, the hiPSC-CMs began to form aggregation structures atop the printed fibers and began to contract synchronously across the entire patches, indicating electrophysiological coupling of the cells (Fig. 2H). Moreover, the beating rate of the hiPSC-CMs on the printed patch was notably similar to that of the monolayer hiPSC-CMs on the seeded well plate (Fig. 2I).

According to previous studies, human mesenchymal stromal cells (hMSCs) have been widely used in coculture with cardiomyocytes and endothelial cells to improve cell viability, myogenesis, angiogenesis, cardiac contractility, and other functions due to their paracrine activity (*34*, *35*). Hence, a triculture of hiPSC-CMs, human endothelial cells (hECs), and hMSCs was performed to fabricate the vascularized cardiac patches. The analysis of cell tracker staining was conducted to investigate the distribution of different cells in the triculture and to optimize the cell ratio in the triculture system based on the calculated fluorescent value. The results demonstrated that when the initial ratio of seeded cells was 4:2:1, the resultant cellular proportion of hiPSC-CMs, hECs, and hMSCs was ~ 30, ~40, and ~30%, respectively, at confluency, which falls within the range of the cellular composition [25 to 35% cardiomyocytes, 40 to 45% endothelial cells, and ~30% supporting cells (i.e., fibroblasts, smooth muscle cells, hematopoietic-derived cells, and others)] of the human heart (Fig. 3A) (*36*, *37*). After 7 days of culture, the printed construct showed a uniform cell distribution and longitudinal alignment of the cells along the fiber direction (Fig. 3B and fig. S3). Autofluorescence images of green fluorescent protein–transfected (GFP^+) hiPSC-CMs on day 7 indicated that the cardiomyocytes exhibited an increased proliferation rate on the patches, as compared to initial seeding on day 1, and were able to generate spontaneous contractions (Fig. 3C and fig. S4). After 7 days of culture, fluorescent image analysis of CD31 [platelet endothelial cell adhesion molecule-1 (PECAM-1)] stained patches revealed that the wave-patterned patch had a higher density of capillary-like hEC distribution along the fibers when compared to the mesh control (Fig. 3D). In our previous studies, we found that the beam-scanning laser is able to cure the ink for the macroarchitectural formation together with the aligned microstructure present on the printed fibers (*16*). Hence, the hECs were easily grown along the fiber direction. Moreover, the iPSC-CMs exhibited an excellent contraction-relaxation behavior along the fibers in the wave-patterned patches, potentially allowing for a local mechanical stimulation on the fiber resident cells, which can help to improve the growth and distribution of hECs. In addition, immunostaining analysis of the cTnI and the marker von Willebrand factor (vWf) indicated that our wave-patterned patches contained a dense network of vascular cells interwoven with hiPSC-CMs distributed over the printed fibers, and the ratio of hiPSC-CMs and hECs was largely retained with ≈45% hiPSC-CMs (Fig. 3, E and F). Furthermore, it has been well established that the electrical activity at the cardiomyocyte membrane is controlled by ion channels and G protein–coupled receptors, which are usually actuated by calcium transients (*38*). The electrophysiological profiles of the cardiac patches demonstrated the generation of typical calcium oscillation waveforms and synchronous beating along with the printed fibers across the entire patches after 3 days (Fig. 3G). Over the next 7 days of culture, the amplitudes of calcium transients gradually increased to a stable state, suggesting the establishment of excellent functional contraction-relaxation and electrophysiological behaviors (Fig. 3, H and I).

Biomechanical stimulation and functional maturation

To enhance the effectiveness of our design, a custom-made bioreactor consisting of a dynamic flow device and a mechanical loading device was constructed to provide a physiologically relevant environment, which could incorporate both mechanical strain and hydrodynamics (Fig. 4A) (*39*). The patches were compressed in the radial direction using positive pressure between the piston and stationary polydimethylsiloxane (PDMS) holder to yield a mechanical loading, which mimics the contractile behavior of the in vivo human heart (fig. S5A). During the dual mechanical stimulation (MS), the applied force was stored in the patch as strain energy, which was then responsible for returning the patch to its original shape. The out-of-plane loading (bending) determines the stretch and recovery of the fibers, while the fluid shear stress regulates cellular orientation (Fig. 4B). Both were applied to the patches and transferred onto the cells to improve the vascularization and myocardial maturation of the resident cells.

After 2 weeks of dynamic culture, we observed a higher expression of mature cardiomyogenic cTnI and angiogenic vWf in MS samples and more longitudinally aligned vascular cells, when compared to the nonstimulated control (Fig. 4C and fig. S5, B and C). In addition, the patches exhibited enhanced sarcomere density and junctions, as identified by the α-actinin and Cx43 expression of the hiPSC-CMs (Fig. 4D and fig. S5, D and E). Cross-sectional images illustrated that the high density of cell assemblies on the wave-patterned patches was evident under MS conditions and these assemblies exhibited a higher expression of desmin and CD31 markers compared to the mesh control (Fig. 4E). This suggests that the specific design of the cardiac patch was able to impede the mechanical force against material deformation in our dynamic system to support repeatable stretch cycles and decrease the negative effect on the cells. Moreover, the assembled hiPSC-CM fibers on the cardiac patch spontaneously and synchronously contracted along with the fiber direction (Fig. 4F and movie S3). However, the entire patch did not exhibit in-plane contraction or macroscopic movement itself due to the high mechanical resistance of the hydrogel material. In general, it was observed that the wave-patterned patch was capable of stretching to a physiologically relevant fiber pattern compared to the mesh design, which could improve cell guidance and elongation along the fiber direction.

Consistent with the immunostaining results, the expression of cardiac-related genes, including genes associated with sarcomeric structure, excitation-contraction coupling, and angiogenesis, was significantly increased on day 14 compared to day 7. These results suggest that there was an increase in maturation of the iPSC-CMs on the printed patches over time (Fig. 4, G to I, table S1, and fig. S6). After the application of the MS, the expression of the MYL2 (myosin light chain 2) and RYR2 (ryanodine receptor 2) genes were significantly increased in our wave-patterned patches on day 14, as compared to the mesh control. This demonstrates that our specific patch design can enhance iPSC-CM contractile and electrical function under MS. Moreover, the angiogenic CD31 gene was also considerably up-regulated on the wave-patterned patches with perfusion culture. In general, the gene expression on day 14 was up to 28-fold higher compared to day 1, and an average of 5.5-fold increase in the expression of maturation genes was observed with the MS condition as compared to

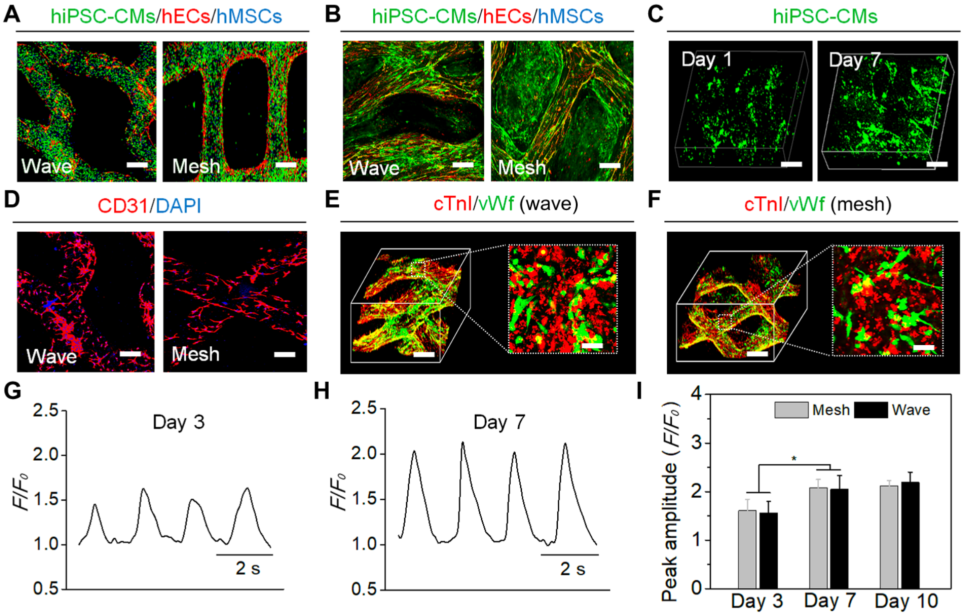

Fig. 3. In vitro characterization of the printed cellularized patches. Cell distribution of tricultured hiPSC-CMs (green), hECs (red), and hMSCs (blue) on the cardiac patches using cell tracker staining after (**A**) 1 day of confluence and (**B**) 7 days of culture. Scale bars, 200 μm. (**C**) Autofluorescence 3D images of GFP$^+$ hiPSC-CMs on the wave-patterned patch on day 1 and day 7. Scale bars, 100 μm. (**D**) Immunostaining of capillary-like hEC distribution (CD31; red) on the hydrogel patches. Scale bars, 200 μm. Immunostaining (3D images) of cTnI (red) and vascular protein (vWf; green) on the (**E**) wave-patterned and (**F**) mesh-patterned patches. Scale bars, 200 μm (3D image) and 20 μm (2D inset). Calcium transients of hiPSC-CMs on the hydrogel patches recorded on (**G**) day 3 and (**H**) day 7. (**I**) Peak amplitude of the calcium transients of hiPSC-CMs on the mesh- and wave-patterned patches on day 3, day 7, and day 10 (means ± SD, $n \geq 30$ cells, $^*P < 0.05$).

the nonstimulated groups. This observation provides further evidence that significantly enhanced cardiac maturation is achievable on the printed patches when specific structural design and physiologically relevant culture conditions are combined.

In vivo implantation and long-term evaluation

Having used the dynamic culture system to enhance the maturation of hiPSC-CMs in vitro, we further investigated the vascularization and myogenic maturation of the printed cardiac patches in vivo. Ischemia-reperfusion (I/R) is a major contributor to the myocardial damage resulting from MI in humans (*40*). Murine models of I/R injury provide an effective means to simulate clinical acute or chronic heart disease for cardiovascular research (*41*, *42*). Hence, a chronic MI model with I/R injury was created to assess the functional effects of cardiac patch implantation (*43*, *44*). The cellularized and acellular patches were implanted onto the epicardium of immunodeficient nonobese diabetic severe combined immunodeficient gamma (NSG) mice and were assessed for long-term development 4 months after implantation. Compared to the classic MI model, our I/R injury model produced a shortened recovery time, less inflammation, and higher survival rates. The patches (4-mm diameter by 600-μm thickness in size) were entirely positioned over the infarcted (ischemia) site of the mouse hearts (Fig. 5, A and B, and movie S4). To assess the direct interaction (structure and cells) between the patch and the host epicardium, we did not apply fibrin glue. After 3 weeks of implantation, optical images showed that the cellularized patches had a firm adhesion to the epicardium regardless of the contractile function of the heart (Fig. 5C). Hematoxylin and eosin (H&E) assessment confirmed the robust epicardial engraftment of the cell-laden patches, which contained high-density cell clusters after 3 weeks (Fig. 5D). Fluorescent images also showed that the GFP$^+$ hiPSC-CMs (green) maintained higher viability after 3 weeks of implantation (Fig. 5E). The immunofluorescence analysis of cTnI and vWf illustrated the existence and development of hiPSC-CMs and hECs on the cellularized patches in the treated region with time. The image results showed that many vascular cells were found spanning the interface of the patch and myocardium and expanded within the myocardial patch (Fig. 5F).

After 10 weeks of implantation, H&E staining results showed that the infarct sizes of the patch groups (~3.8 ± 0.7%) were smaller than the MI-only control (~8.4 ± 1.1%), suggesting that the patch can provide mechanical support to effectively prevent LV remodeling (Fig. 5G and fig. S7A). The images and videos of the cardiac magnetic resonance imaging (cMRI) demonstrated that the implanted patch was able to contract and relax with the heartbeat of the mouse and also confirmed its excellent structural durability along with evident blood perfusion from the heart to the patch (Fig. 5H and movie S5). Fluorescent images also showed that the GFP$^+$ hiPSC-CMs (green) maintained higher viability after 10 weeks of implantation (fig. S7B). hiPSC-CMs with cTnI$^+$-expressing capillaries (vWf$^+$) were observed in the patches, where the lumen structure of neovessels was also clearly visible (Fig. 6A). Together, these results indicated that epicardially implanted patches exhibited robust survival and vascularization in vivo. Moreover, a high density of capillaries identified by human-specific CD31 expression was observed within the cellularized patches, suggesting that the implanted hECs and hMSCs increased the vessel formation throughout the patch in vivo (Fig. 6B).

By 4 months, H&E staining results showed a higher cell density and smaller infarct area (~5.6 ± 1.5%) in the cellularized patch compared to the acellular patch and MI groups (~14.3 ± 2.3%; fig. S7C).

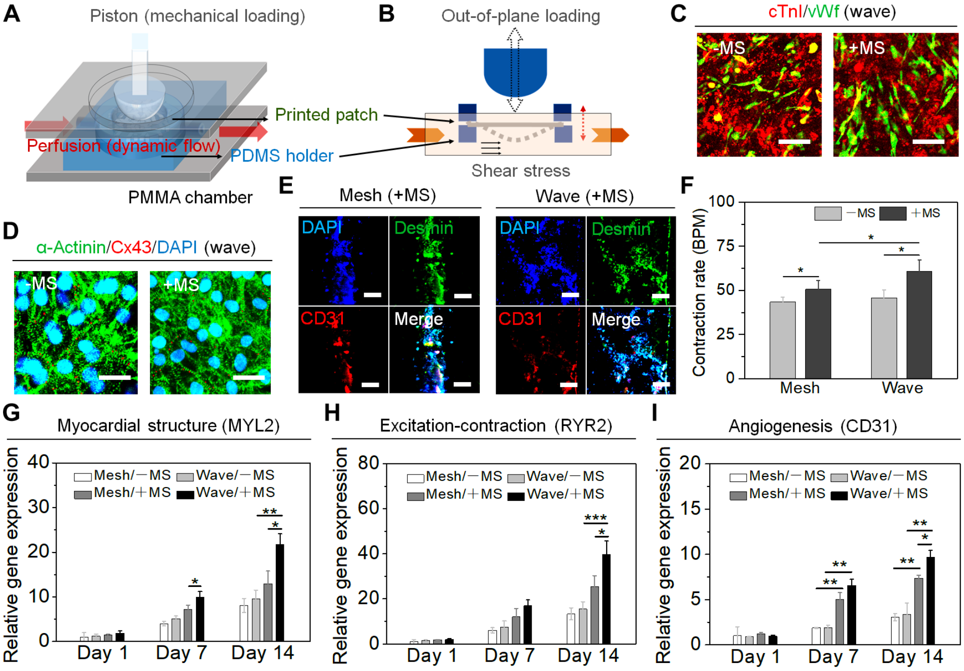

Fig. 4. Biomechanical stimulation and functional maturation of printed cellularized patches. (**A**) Schematic illustration of a custom-made bioreactor to apply dual MS for the maturation of engineered cardiac tissue. PMMA, polymethylmethacrylate. (**B**) Both the out-of-plane loading and fluid shear stress applied to the patches. (**C**) Immunostaining of cTnI (red) and vWf (green) on the wave-patterned patch under MS condition (+MS) versus nonstimulated control (−MS). Scale bars, 50 μm. (**D**) Immunostaining of the α-actinin (green) and Cx43 (red) on the wave-patterned patch under MS condition (+MS) versus nonstimulated control (−MS). Scale bars, 20 μm. (**E**) Cross-sectional immunostaining of the sarcomeric structure (Desmin; green) and vascular CD31 (red) on the patches under MS condition (+MS). Scale bars, 50 μm. (**F**) The beating rate of hiPSC-CMs on the printed patches under MS condition (+MS) versus nonstimulated control (−MS) on day 14 (means ± SD, $n \geq 6$, $^*P < 0.05$). BPM, beats per minute. Relative gene expression of (**G**) myocardial structure [myosin light chain 2 (MYL2)], (**H**) excitation-contraction coupling [ryanodine receptor 2 (RYR2)], and (**I**) angiogenesis (CD31) on the patches under MS condition (+MS) versus nonstimulated control (−MS) on day 1, day 7, and day 14 (means ± SD, $n \geq 9$, $^*P < 0.05$, $^{**}P < 0.01$, and $^{***}P < 0.001$).

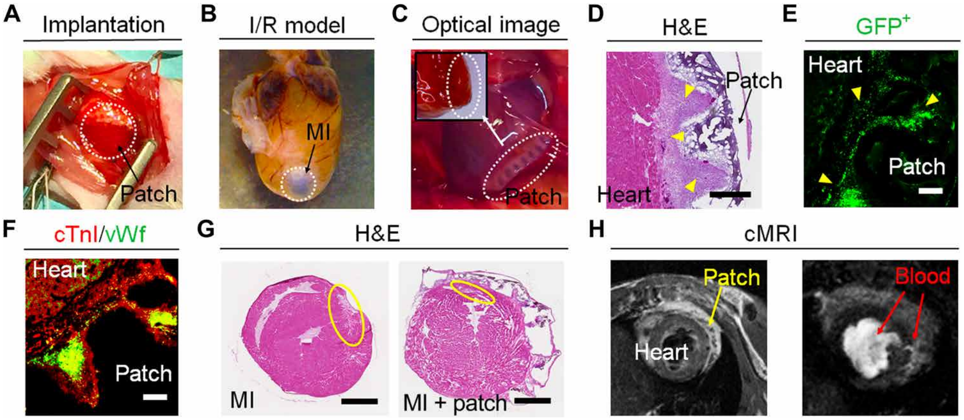

Fig. 5. In vivo implantation and long-term evaluation of 4D patches. (**A**) Optical image of surgical implantation of the patch. (**B**) Optical image of a heart I/R MI model after 4 months. (**C**) Optical image of the implanted cellularized patch at week 3, exhibiting a firm adhesion (inset). (**D**) H&E image of the cellularized patch at week 3, demonstrating the cell clusters with a high density (yellow arrowhead). Scale bar, 400 μm. (**E**) Fluorescent image of (GFP^+) iPSC-CMs on the patch at week 3, showing a high engraftment rate (yellow arrowhead). Scale bar, 100 μm. (**F**) Immunostaining of cTnI (red) and vWf (green) on the cellularized patch at week 3. Scale bar, 100 μm. (**G**) H&E images of mouse MI hearts without treatment (MI) and with cellularized patch (MI + patch) at week 10. Infarct area after MI (yellow circles). Scale bars, 800 μm. (**H**) Cardiac magnetic resonance imaging (cMRI) images of a mouse heart with patch at week 10. Left (spin echo): the position of the heart and implanted patch. Right (cine): the blood (white color) perfusion from the heart to the patch. Photo credit: Haitao Cui, GWU.

The GFP^+ fluorescent results demonstrated that the hiPSC-CMs retained high engraftment rates (fig. S7D). Similar to what was observed at 10 weeks, the cellularized patch had a strong integration within the epicardium, whereas the cell-free patch had a weak adhesion by month 4. In addition, the cMRI images also illustrated that the implanted patch had an excellent connection with the mouse heart (fig. S7E). The positive expression of mature cTnI further indicated the presence of advanced structural maturation of the hiPSC-CMs in the treated region, and the capillaries were also substantially identified by the vWf staining in the cell-laden patch groups (Fig. 6C).

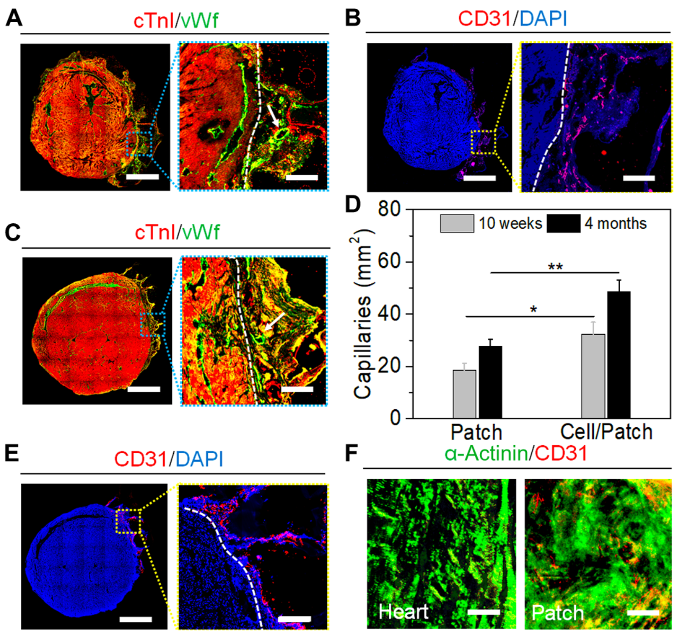

Fig. 6. In vivo implantation and long-term evaluation of 4D patches (continuous). (**A**) Immunostaining of cTnI (red) and vWf (green) on the cellularized patch at week 10. Scale bar, 800 μm. Border of the heart (white dashed line) and capillary lumen (white arrow). Scale bar (enlarged), 100 μm. (**B**) Immunostaining of human-specific CD31 (red) on the cellularized patch at week 10, showing the generated capillaries by hECs. Scale bar, 800 μm. Border of the heart (white dashed line). Scale bar (enlarged), 100 μm. (**C**) Immunostaining of cTnI (red) and vWf (green) on the cellularized patch for 4 months, showing the increased density of the vessels. Scale bar, 800 μm. Border of the heart (white dashed line) and capillary lumen (white arrow). Scale bar (enlarged), 100 μm. (**D**) Quantification of capillaries with vWf staining data for 10 weeks and 4 months (means ± SD, $n \geq 6$, $^*P < 0.05$ and $^{**}P < 0.01$). (**E**) Immunostaining of human-specific CD31 (red) on the cellularized patch for 4 months. Scale bar, 800 μm. Border of the heart (white dashed line). Scale bar (enlarged), 100 μm. (**F**) Immunostaining of α-actinin (green) and human-specific CD31 (red) on the cellularized patch at month 4. Scale bars, 50 μm.

The images also demonstrated more progressive implant vascularization with a 1.5-fold increase in blood vessel density after 4 months of implantation, when compared to cell-free controls (Fig. 6D). The data were counted by five randomly selected fields in each heart. However, the fraction of humanized vessels was not significantly increased, as identified by the human-specific CD31 staining (Fig. 6E). Therefore, the increased vascularization and vascular remodeling in vivo likely originated from the host vessel ingrowth as opposed to the implanted human vessels at the initial stage of implantation. However, differing from the in vitro results, the cross-sectional images of the implants did not exhibit substantial sarcomeric structure (identified by α-actinin) when compared to the native cardiac tissue (Fig. 6F). It can be observed that the cell aggregation in the vertical direction showed a disordered assembly and 3D stacking behavior. Overall, these results demonstrated that the printed patches underwent progressive vascularization, largely remained on the epicardial surface of the LV over the 4-month implantation period, and effectively covered all of the infarcted area. Cardiac function was also evaluated at different time points after injury via cMRI assessments. The LV ejection fraction of all patch groups (~64.1 ± 3.5%) was higher than the MI-only group (~56.1 ± 1.5%); however, there was no difference observed between the cellularized patch group and the cellular group.

DISCUSSION

MI is a leading cause of morbidity and mortality worldwide. The hiPSC-CMs provide a potentially unlimited source for cardiac tissue regeneration, as they are able to recapitulate many of the physiological, structural, and genetic properties of human primary cardiomyocytes and heart tissue (*13*). Current methods for the treatment of MI largely involve injecting cardiomyocytes directly into the epicardial infarct zone; however, because of the limited engraftment capacity of the injected cardiomyocytes, injection therapies are not fully satisfactory in restoring cardiac functionality (*13*). Several studies have been performed with hiPSC-CMs to generate functional cardiac tissue constructs using tissue engineering techniques (*7*, *10*). However, the physiological features of hiPSC-CMs are more sensitive to the physicochemical and bioactive properties of the scaffolds in which they reside. Compared to synthetic polymers, natural polymer-based hydrogels can provide a more favorable matrix for the growth and differentiation of cardiomyocytes (*7*). However, limitations of structural design and manufacturing techniques, as well as the low mechanical strength and weak processability of hydrogel-based patches, still make their clinical application challenging.

As a proof of concept, a physiologically adaptable 4D cardiac patch, which recapitulates the architectural and biological features of the native myocardial tissue, has been printed using a beam-scanning SL printing technique. The smart patches provided mechanical support, a physiologically tunable structure, and a suitable matrix environment (elasticity and bioactivity) for cell implantation. Successful vascularization of the patches allowed for the continued metabolic demand of hiPSC-CMs and permitted them to remain both viable and functional throughout the in vivo study. Robust engraftment and development of the implanted patches were further confirmed using a more clinically relevant and mechanically realistic environment. The study results showed that the anisotropic mechanical adaption of the printed patches improved the maturation of cardiomyocytes and vascularization in vitro under MS. After implantation into the murine MI model, the printed patches exhibited high levels of in vivo cell engraftment and vascularization.

In a previous study, an engineered auxetic design was developed to give a cardiac patch a negative Poisson's ratio, providing it with the ability to conform to the demanding mechanics of the heart (*31*). Here, we further propose and develop a 4D physiologically adaptable design for a cardiac patch, which includes hierarchical macro- and microstructural transformations attuned to the mechanically dynamic process of the beating heart. Therein, a physiological adaptation is evident in the response of cells (or genes) to the microenvironmental change. Similarly, the adaptive responses of the resident cells on the scaffolds to replicate the native microenvironment are crucial for the in vivo integration of engineered tissue with and the host tissue after implantation. In addition, a highly biomimetic in vitro culture system was developed with dynamic perfusion and mechanical loading to enhance cardiac maturation. Overall, the current work has several unique features: (i) a greatly improved mechanical stretchability of the hydrogel patches; (ii) a triculture of hiPSC-CMs, hMSCs, and hECs, which is necessary to obtain a complex cardiac tissue; (iii) an application of in vitro dual MS by which to improve cardiac maturation; and (iv) in vivo long-term development of the printed patches in a murine chronic MI model to evaluate the potential therapeutic effect.

Although several studies have shown that cell transplantation can greatly improve cardiac function in the MI model, no substantial evidence supporting these improvements in cardiac function was found in the current study. In the MS culture studies, it was observed that the entire patch did not exhibit in-plane contraction. The high mechanical resistance of the hydrogel could be a reason as to why the patches did not significantly enhance cardiac function in vivo. Moreover, as is known, the implanted human cardiomyocytes exhibit different beating frequencies and other biological features within the host mouse heart (*13*, *45*, *46*). Hence, integrated functional repair was not observed in this study. Differing from the hypothesis of the functional enhancement, the in vivo results revealed that the enhanced cardiomyogenesis and neovascularization of humanized patches did not significantly improve the cardiac function of the MI mice. The patches provided cellularized niche conditions so that most of the implanted cardiomyocytes were alive, although they still exhibited immature 3D sarcomeric organization. Moreover, the neovascularization effects of the cell-laden patches at the infarct region were also confirmed, suggesting that paracrine effects appear to be a major contributing factor. Although there was a lack of functional integration between humanized patches with the hearts of the host mice, the printed patches exerted no adverse effects on the host cardiac function or vulnerability to arrhythmias. The cell transplantation improved the cellularized environment in the infarct area by, at least in part, promoting angiogenesis and increasing cell retention. The multiple cell transplantation with a high density of hiPSC-CMs retention in the murine MI model suggests that this goal may have been at least partially achieved. While applying humanized grafts to infarcted rodent hearts would likely confirm the paracrine effects, large animal studies are warranted to further evaluate the therapeutic efficacy toward a potential clinical use.

In the future, a physiologically relevant large animal study, such as a porcine or nonhuman primate MI model, will serve as a more realistic means to study cardiac patch engraftment (*42*, *46*). Moreover, developments in advanced printing techniques will enable the development of thick, scale-up ready myocardial tissue, which will play a prominent role in the ultimate success of clinical cardiac engineering therapies. In general, the developed cardiac patch has a great potential to provide a desired therapeutic effect on the in vitro maturation and in vivo retention of hiPSC-CMs, based on the previously unidentified engineering design and manufacturing process.

MATERIALS AND METHODS

Experimental design

These studies were designed to evaluate the concept of a 4D cell-laden cardiac patch with physiological adaptability as a potential method for the treatment of MI. To evaluate this technology, we tricultured hiPSC-CMs, hMSCs, and hECs to obtain a complex cardiac tissue and also applied in vitro dual MS to replicate the physiologically relevant conditions for the improvement of regenerated myocardial function. A 4-month in vivo study was conducted to assess the performance of our 4D cell-laden cardiac patches, where the animals were randomly assigned to different experimental groups before the experiments. The sample size and power calculation were determined on the basis of our experience with the experimental models and the anticipated biological variables. Typically, the power is 0.8, and the significance level is 0.05 when the effect size is determined by the minimum sample difference divided by the SD (GPower 3.1). All experiments were blinded and replicated. The sample sizes and replicates are shown in the figure legends.

Preparation of photocurable GelMA/PEGDA inks

Ten grams of gelatin (type A, Sigma-Aldrich) was dissolved in 100 ml of deionized water with stirring at 80°C. Next, 5 ml of methacrylic anhydride was added dropwise into the gelatin solution. After reaction at 80°C for 3 hours, the reactant was dialyzed in deionized water for 5 days at 40°C to remove any excess methacrylic acid. The GelMA solid product was finally obtained through lyophilization. The ink solutions consisted of GelMA [with concentrations of 0, 5, 10, 15, or 20 weight % (wt %)], 1 wt % 2-hydroxy-4′-(2-hydroxyethoxy)-2-methylpropiophenone (Irgacure 2959, photoinitiator), and PEGDA (Mn = 700; Sigma-Aldrich; with concentration of 0, 5, 10, 15, and 20 wt %). Solutions were prepared using a 1× phosphate-buffered saline (PBS) solution.

CAD design of physiologically adaptable architecture

Our 3D computational myocardium model was programmed on the basis of DTI results and was simplified to the basic geometry to replicate the fiber orientation of the native myocardium. The wave (or hexagonal) microstructure was configured with different diameter fibers and fiber angels between each layer, while the mesh microstructure served as a control. To optimize the fiber design, wave or mesh architectures with side lengths of 100, 200, and 400 μm and internal angles (θ) of 30°, 45°, and 60° between each layer were designed with two, four, and eight layers, respectively. All cardiac construct models were saved as .stl files, processed using the Slic3er software package, and were transferred to the 3D printer. Representative CAD models of the constructs were calculated and predicted for surface area, porosity, and other structural characteristics.

SL-based printing of cardiac patches

Printed cardiac patches were manufactured using our customized table-top beam-scanning SL printer, which is based on the existing Printrbot rapid prototyping platform. This system consists of a movable stage and a 110-μm fiber optic-coupled solid-state ultraviolet (355 nm) laser mounted on an X-Y tool head for three-axis motion. The laser scans and solidifies the top layer of ink in a reservoir, and a movable platform lowers the construct further into the ink, covering it with the next material layer. For this study, the effective spot size of the emitted light was 150 ± 50 μm and had an energy output of ~20 uJ at 20 kHz. The ability to alter the frequency of the pulsed signal facilitates power control at the material surface ranging from ≈40 to 110 mW.

Characterization

Different stacked architectures with fiber widths of 100, 200, and 400 μm; fill densities of 20, 40, and 60%; and fiber angels of 30°, 45°, and 60° between each layer were manufactured with two, four, and eight layers, respectively. The printing accuracy of the patterns was quantified by the mean trajectory error (E_t) compared to the designed shape. $E_t = \frac{1}{n}\sum_{i=0}^{n}\sqrt{(x(i)-x_t(i))^2+(y(i)-y_t(i))^2}$, where $n \geq 20$ is the number of data points collected. Compressive and tensile mechanical properties were measured with an MTS criterion universal testing system equipped with a 100-N load cell (MTS Systems Corporation). For compressive testing, the printed patches (2 cm by 2 cm) having different microstructures were placed on the tester. The crosshead speed was set to 2 mm/min, and Young's modulus was calculated from the linear region of the compressive stress-strain curves. For the tensile testing, the samples were mounted on to custom-made copper hooks affixed to the tester and were pulled at a rate of 1 mm/min to a maximum strain of 20%. Young's modulus was calculated from the linear portion of the tensile stress-strain curve. In addition, the representative uniaxial tensile stress-strain plots for the latitudinal and longitudinal specimens of myocardial constructs were used to evaluate the anisotropic mechanical properties. The swelling behavior was evaluated by quantifying the weight gain after equilibrium swelling. The printed samples were immersed in PBS at 37°C for 7 days. The swelling ratios of hydrogel matrices were calculated as equilibrium mass swelling ratio (SR). SR = $(w_t - w_0)/w_0 \times 100\%$, where w_0 is the original weight of printed samples and w_t is the equilibrium weight of samples after swelling.

Cell culture

hiPSC-CMs and GFP$^+$ hiPSC-CMs were cultured in cardiomyocyte basic medium using the same protocol developed by our collaborators at the NHLBI (*33*). hECs (human umbilical vein endothelial cells; Thermo Fisher Scientific) were cultured in endothelial growth medium consisting of Medium 200 and low-serum growth supplement. hMSCs (harvested from normal human bone marrow, Texas A&M Health Science Center, Institute for Regenerative Medicine) were cultured in mesenchymal stem cell growth medium consisting of α–minimum essential medium, 20% fetal bovine serum, 1% L-glutamine, and 1% penicillin/streptomycin. All experiments were performed under standard cell culture conditions (in a humidified, 37°C, 95% air/5% CO_2 environment) with hECs and hMSCs of six cell passages or less.

Cellularized cardiac patches and culture in vitro

After the patches were printed, iPSC-CMs, hECs, and hMSCs with different ratios were seeded on the patch constructs (the surface of the patch was precoated with a thin layer of Matrigel, Corning). The tricultured cardiac patches were maintained in the mixed medium at a 1:1:1 ratio for further characterization and in vitro cell study. hECs and hMSCs were prestained with CellTracker Orange CMRA Dye and CellTracker Blue CMAC Dye (Molecular Probes) and were then seeded onto the constructs. After 1, 3, and 7 days of coculture, cells were imaged using a Zeiss 710 confocal microscope. Cell proliferation on days 1, 3, and 7 were quantified using a cholecystokinin-8 solution [10% (v/v) in medium; Dojindo]. After 2 hours of incubation, the absorbance values were measured at 570 and 600 nm on a photometric plate reader (Thermo Fisher Scientific). The spreading morphology and arrangement of hMSCs and hECs were characterized using the double staining of F-actin (red, Texas Red; 1:200) and nuclei [blue, 4,6-diamidino-2-phenylindole dihydrochloride (DAPI), Thermo Fisher Scientific; 1:1000].

Biomechanical stimulation in a bioreactor device

A customized bioreactor system consisting of a mechanical loading device and a dynamic flow device was used to culture our cell-laden constructs. The dynamic flow device is composed of four parts: a perfusion chamber, a flow controller, a nutrient controller, and a gas controller (5% CO_2/95% air). The culture medium was perfused through the constructs using a digital peristaltic pump (Masterflex, Cole-Parmer) over the whole experimental period, which facilitated the efficient transfer of nutrients and oxygen. A shear stress was set at 10 dynes/cm^2 (which is within the range of the shear stress observed in microcirculation), and a flow rate of 8.4 ml/min was selected (the viscosity of medium is ~7.8×10^{-4} N·s/m^2) (*47*, *48*). A PDMS holder was used to both firmly mount the patches within a polymethylmethacrylate chamber and to maintain the patch structure during cell culturing and MS to prevent undesired movement and damage. The patches were compressed at the speed of 60 times/min in the radial direction using positive pressure between the piston and the stationary holder to yield the mechanical force. The calculated (preload) contractile force per unit area was ~50 mN/mm^2 along the fiber direction to match those in the native cardiac tissue. The cardiac constructs were placed in the bioreactor system and incubated at 37°C for 7 and 14 days.

Cell immunostaining

After 1 and 2 weeks of culture, cellular functions including cardiomyogenesis and angiogenesis were assessed using an immunofluorescence method. After the predetermined period, the cell-laden constructs were fixed with formalin for 20 min. The samples were permeabilized in 0.1% Triton X-100 for 15 min and were then incubated with a blocking solution [containing 1% bovine serum albumin, 0.1% Tween 20, and 0.3 M glycine in PBS] for 2 hours. The cells were then incubated with primary antibodies at 4°C overnight. After incubation with primary antibodies, secondary antibodies were introduced to the samples in the dark for 2 hours at room temperature, followed by incubation with a DAPI (1:1000) solution for 5 min. All images were obtained using the confocal microscope, and protein quantifications were performed using ImageJ (*49*). In addition, the immunostaining analysis was performed with sliced fragments that were cut with a cryostat microtome. The primary antibodies that were used for our study were purchased from Abcam and included anti–α-actinin (1:500), anti–human-specific CD31 (human-specific PECAM-1; 1:500), anti-desmin (1:1000), anti-Cx43 (1:1000), anti-cTnI (1:500), and anti-vWf (1:1000). The secondary antibodies were purchased from Thermo Fisher Scientific and included anti-mouse Alexa Fluor 594 (1:1000) and goat anti-rabbit Alexa Fluor 488 (1:1000).

In vitro analysis of contractility

To evaluate the functional beating behavior, iPSC-CMs were observed and recorded using the inverted microscope and confocal microscopy. The Ca^{2+} that triggers contraction comes through the sarcolemma and plays an important role in excitation-contraction coupling of the heart beating. After the predetermined period, intracellular calcium transients were recorded under the fluorescent microscope at a wavelength of 494 nm over 30 to 120 s. Movies were analyzed with an ImageJ software to measure the fluorescence intensities for two to eight regions of interest (F) and for three to eight background regions (F_0) per acquisition.

Gene expression analysis

The cardiac tissue construct–related gene expression was analyzed by a real-time quantitative reverse transcription polymerase chain reaction (RT-PCR) assay. Specifically, myocardial structure [cTnI (TNNI3), cTnT (TNNI2), MYL2, MYL7, myosin heavy chain 6 (MYH6), MYH7, and α-actinin 2 (ACTN2)], excitation-contraction coupling (calsequestrin 2, RYR2, phospholamban, sodium/calcium exchanger 1, and adenosine triphosphatase sarcoplasmic/endoplasmic reticulum

Ca^{2+} transporting 2), and angiogenic genes (vWf and CD31) were studied to detect the cardiomyocyte and vascular maturation processes in the constructs. The primers that were used are shown in the Supplementary Materials (table S1). Briefly, the total RNA content was extracted using TRIzol reagent (Life Technologies). The total RNA purity and concentration were determined using a microplate reader [optical density at 260/280 nm within 1.8 to 2.0). The RNA samples were then reverse-transcribed to complementary DNA using the Prime Script RT Reagent Kit (Takara). RT-PCR was then performed on the CFX384 Real-Time System (Bio-Rad) using SYBR Premix Ex Taq according to the manufacturer's protocol. The gene expression levels of the target genes were normalized against the housekeeping gene glyceraldehyde 3-phosphate dehydrogenase. The relative gene expression was normalized against the control group to obtain the relative gene expression fold values, which were calculated via the $2^{-\Delta\Delta Ct}$ method.

I/R model and in vivo evaluation

The in vivo development of the printed cellularized constructs was evaluated using a xenograft model of transplantation into 6-week-old NSG mice. All the animal experiments were approved by the Institutional Animal Care and Use Committee of the NHLBI. A method of random and blinded group allocation was applied to our animal experiments. The murine model with chronic MI was created via an I/R procedure to analyze implanted cell development, remodeling, and infarction treatment for 4 months. The printed cellularized patches (4-mm diameter by 600-μm thickness in size) were prepared in sterile conditions and were surgically implanted into the LV ischemic area of each NSG mouse through a limited left lateral thoracotomy. The acellular patch and MI-only groups served as controls. At different time points after implantation, cMRI was performed to visualize the beating heart and to evaluate the structural/functional parameters, which included the ejection fraction, end-systolic volume, end-diastolic volume, stroke volume, and cardiac output, among others. Last, animals were euthanized, and the specimens, along with the adjacent tissues, were collected for further examination.

Histological examination

Histology was used to qualitatively examine the samples at different time points and included the examination of cellular cytoplasm, red blood cells, and cell distributions. The samples were fixed in formalin, processed, and were embedded in optimal cutting temperature compound for cryosection histology. The samples were cut into 5- to 10-μm slides. The mean infarct size was also calculated through the histologic studies. The infarct size was expressed as the percentage of the affected myocardial area (necrosis + inflammatory tissue) in all myocardial areas analyzed, with infarct area % = infarct area × 100/total myocardial area. Immunostaining was used to evaluate the in vivo cardiomyogenesis and angiogenesis of the implants. The antibodies were used in a manner similar to the in vitro study. The number of neovessels, including sprouted capillaries, was counted per section, and a total of five sections per sample were analyzed. All of the slide analyses were performed using the ImageJ software.

Statistical analysis

All data are presented as the means ± SD. A one-way analysis of variance (ANOVA) with Tukey's test was used to verify statistically significant differences among groups via Origin Pro 8.5, with $P < 0.05$ being statistically significant ($^{\#}$, $^{*}P < 0.05$; $^{\#\#}$, $^{**}P < 0.01$; $^{\#\#\#}$, $^{***}P < 0.001$).

SUPPLEMENTARY MATERIALS

Supplementary material for this article is available at http://advances.sciencemag.org/cgi/content/full/6/26/eabb5067/DC1

View/request a protocol for this paper from *Bio-protocol*.

REFERENCES AND NOTES

1. M. A. Laflamme, C. E. Murry, Heart regeneration. *Nature* **473**, 326–335 (2011).
2. H. Cui, S. Miao, T. Esworthy, X. Zhou, S.-J. Lee, C. Liu, Z.-X. Yu, J. P. Fisher, M. Mohiuddin, L. G. Zhang, 3D bioprinting for cardiovascular regeneration and pharmacology. *Adv. Drug Deliv. Rev.* **132**, 252–269 (2018).
3. F. Weinberger, I. Mannhardt, T. Eschenhagen, Engineering cardiac muscle tissue: A maturating field of research. *Circ. Res.* **120**, 1487–1500 (2017).
4. B. M. Ogle, N. Bursac, I. Domian, N. F. Huang, P. Menasché, C. E. Murry, B. Pruitt, M. Radisic, J. C. Wu, S. M. Wu, J. Zhang, W.-H. Zimmermann, G. Vunjak-Novakovic, Distilling complexity to advance cardiac tissue engineering. *Sci. Transl. Med.* **8**, 342ps313 (2016).
5. R. Gaetani, D. A. Feyen, V. Verhage, R. Slaats, E. Messina, K. L. Christman, A. Giacomello, P. A. Doevendans, J. P. Sluijter, Epicardial application of cardiac progenitor cells in a 3D-printed gelatin/hyaluronic acid patch preserves cardiac function after myocardial infarction. *Biomaterials* **61**, 339–348 (2015).
6. B. Schoen, R. Avrahami, L. Baruch, Y. Efraim, I. Goldfracht, O. Elul, T. Davidov, L. Gepstein, E. Zussman, M. Machluf, Electrospun extracellular matrix: Paving the way to tailor-made natural scaffolds for cardiac tissue regeneration. *Adv. Funct. Mater.* **27**, 1700427 (2017).
7. G. Camci-Unal, N. Annabi, M. R. Dokmeci, R. Liao, A. Khademhosseini, Hydrogels for cardiac tissue engineering. *NPG Asia Mater.* **6**, e99 (2014).
8. A. Mathur, Z. Ma, P. Loskill, S. Jeeawoody, K. E. Healy, In vitro cardiac tissue models: Current status and future prospects. *Adv. Drug Deliv. Rev.* **96**, 203–213 (2016).
9. K. K. Hirschi, S. Li, K. Roy, Induced pluripotent stem cells for regenerative medicine. *Annu. Rev. Biomed. Eng.* **16**, 277–294 (2014).
10. H. Chen, A. Zhang, J. C. Wu, Harnessing cell pluripotency for cardiovascular regenerative medicine. *Nat. Biomed. Eng.* **2**, 392–398 (2018).
11. L. Gao, M. E. Kupfer, J. P. Jung, L. Yang, P. Zhang, Y. Da Sie, Q. Tran, V. Ajeti, B. T. Freeman, V. G. Fast, P. J. Campagnola, B. M. Ogle, J. Zhang, Myocardial tissue engineering with cells derived from human-induced pluripotent stem cells and a native-like, high-resolution, 3-dimensionally printed scaffold. *Circ. Res.* **120**, 1318–1325 (2017).
12. I. Y. Shadrin, B. W. Allen, Y. Qian, C. P. Jackman, A. L. Carlson, M. E. Juhas, N. Bursac, Cardiopatch platform enables maturation and scale-up of human pluripotent stem cell-derived engineered heart tissues. *Nat. Commun.* **8**, 1825 (2017).
13. J. Zhang, W. Zhu, M. Radisic, G. Vunjak-Novakovic, Can we engineer a human cardiac patch for therapy? *Circ. Res.* **123**, 244–265 (2018).
14. H. Cui, M. Nowicki, J. P. Fisher, L. G. Zhang, 3D bioprinting for organ regeneration. *Adv. Healthc. Mater.* **6**, 1601118 (2017).
15. S. Miao, H. Cui, M. Nowicki, L. Xia, X. Zhou, S.-J. Lee, W. Zhu, K. Sarkar, Z. Zhang, L. G. Zhang, Stereolithographic 4D bioprinting of multiresponsive architectures for neural engineering. *Adv. Biosyst.* **2**, 1800101 (2018).
16. S. Miao, H. Cui, M. Nowicki, S.-J. Lee, J. Almeida, X. Zhou, W. Zhu, X. Yao, F. Masood, M. W. Plesniak, M. Mohiuddin, L. G. Zhang, Photolithographic-stereolithographic-tandem fabrication of 4D smart scaffolds for improved stem cell cardiomyogenic differentiation. *Biofabrication* **10**, 035007 (2018).
17. X. Sun, W. Altalhi, S. S. Nunes, Vascularization strategies of engineered tissues and their application in cardiac regeneration. *Adv. Drug Deliv. Rev.* **96**, 183–194 (2016).
18. K. L. Coulombe, V. K. Bajpai, S. T. Andreadis, C. E. Murry, Heart regeneration with engineered myocardial tissue. *Annu. Rev. Biomed. Eng.* **16**, 1–28 (2014).
19. G. C. Engelmayr Jr., M. Cheng, C. J. Bettinger, J. T. Borenstein, R. Langer, L. E. Freed, Accordion-like honeycombs for tissue engineering of cardiac anisotropy. *Nat. Mater.* **7**, 1003–1010 (2008).
20. D. D. Streeter Jr., H. M. Spotnitz, D. P. Patel, J. Ross Jr., E. H. Sonnenblick, Fiber orientation in the canine left ventricle during diastole and systole. *Circ. Res.* **24**, 339–347 (1969).
21. D. Rohmer, A. Sitek, G. T. Gullberg, Reconstruction and visualization of fiber and laminar structure in the normal human heart from ex vivo diffusion tensor magnetic resonance imaging (DTMRI) data. *Invest. Radiol.* **42**, 777–789 (2007).
22. F. Pashakhanloo, D. A. Herzka, H. Ashikaga, S. Mori, N. Gai, D. A. Bluemke, N. A. Trayanova, E. R. McVeigh, Myofiber architecture of the human atria as revealed by submillimeter diffusion tensor imaging. *Circ. Arrhythm. Electrophysiol.* **9**, e004133 (2016).
23. A. A. Giannopoulos, D. Mitsouras, S.-J. Yoo, P. P. Liu, Y. S. Chatzizisis, F. J. Rybicki, Applications of 3D printing in cardiovascular diseases. *Nat. Rev. Cardiol.* **13**, 701–718 (2016).
24. A. Korolj, E. Y. Wang, R. A. Civitarese, M. Radisic, Biophysical stimulation for in vitro engineering of functional cardiac tissues. *Clin. Sci. (Lond.)* **131**, 1393–1404 (2017).

25. Z. Zhao, J. Wu, X. Mu, H. Chen, H. J. Qi, D. Fang, Origami by frontal photopolymerization. *Sci. Adv.* **3**, e1602326 (2017).
26. H. Cui, W. Zhu, M. Nowicki, X. Zhou, A. Khademhosseini, L. G. Zhang, Hierarchical fabrication of engineered vascularized bone biphasic constructs via dual 3D bioprinting: Integrating regional bioactive factors into architectural design. *Adv. Healthc. Mater.* **5**, 2174–2181 (2016).
27. S. Miao, W. Zhu, N. J. Castro, M. Nowicki, X. Zhou, H. Cui, J. P. Fisher, L. G. Zhang, 4D printing smart biomedical scaffolds with novel soybean oil epoxidized acrylate. *Sci. Rep.* **6**, 27226 (2016).
28. T. Jiao, R. J. Clifton, G. L. Converse, R. A. Hopkins, Measurements of the effects of decellularization on viscoelastic properties of tissues in ovine, baboon, and human heart valves. *Tissue Eng. Part A* **18**, 423–431 (2012).
29. J. M. Lee, S. L. Sing, E. Y. S. Tan, W. Y. Yeong, Bioprinting in cardiovascular tissue engineering: A review. *Int. J. Bioprinting.* **2**, 136–145 (2016).
30. S. Lee, V. Serpooshan, X. Tong, S. Venkatraman, M. Lee, J. Lee, O. Chirikian, J. C. Wu, S. M. Wu, F. Yang, Contractile force generation by 3D hiPSC-derived cardiac tissues is enhanced by rapid establishment of cellular interconnection in matrix with muscle-mimicking stiffness. *Biomaterials* **131**, 111–120 (2017).
31. M. Kapnisi, C. Mansfield, C. Marijon, A. G. Guex, F. Perbellini, I. Bardi, E. J. Humphrey, J. L. Puetzer, D. Mawad, D. C. Koutsogeorgis, D. J. Stuckey, C. M. Terracciano, S. E. Harding, M. M. Stevens, Auxetic cardiac patches with tunable mechanical and conductive properties toward treating myocardial infarction. *Adv. Funct. Mater.* **28**, 1800618 (2018).
32. M. Castilho, A. van Mil, M. Maher, C. H. G. Metz, G. Hochleitner, J. Groll, P. A. Doevendans, K. Ito, J. P. G. Sluijter, J. Malda, Melt electrowriting allows tailored microstructural and mechanical design of scaffolds to advance functional human myocardial tissue formation. *Adv. Funct. Mater.* **28**, 1803151 (2018).
33. Y. Lin, K. L. Linask, B. Mallon, K. Johnson, M. Klein, J. Beers, W. Xie, Y. Du, C. Liu, Y. Lai, J. Zou, M. Haigney, H. Yang, M. Rao, G. Chen, Heparin promotes cardiac differentiation of human pluripotent stem cells in chemically defined albumin-free medium, enabling consistent manufacture of cardiomyocytes. *Stem Cells Transl. Med.* **6**, 527–538 (2017).
34. E. Marbán, A mechanistic roadmap for the clinical application of cardiac cell therapies. *Nat. Biomed. Eng.* **2**, 353–361 (2018).
35. V. F. Segers, R. T. Lee, Stem-cell therapy for cardiac disease. *Nature* **451**, 937–942 (2008).
36. P. Zhou, W. T. Pu, Recounting cardiac cellular composition. *Circ. Res.* **118**, 368–370 (2016).
37. A. R. Pinto, A. Ilinykh, M. J. Ivey, J. T. Kuwabara, M. L. D'Antoni, R. Debuque, A. Chandran, L. Wang, K. Arora, N. A. Rosenthal, M. D. Tallquist, Revisiting cardiac cellular composition. *Circ. Res.* **118**, 400–409 (2016).
38. S.-S. Zhang, R. M. Shaw, Multilayered regulation of cardiac ion channels. *Biochim. Biophys. Acta* **1833**, 876–885 (2013).
39. H. Parsa, K. Ronaldson, G. Vunjak-Novakovic, Bioengineering methods for myocardial regeneration. *Adv. Drug Deliv. Rev.* **96**, 195–202 (2016).
40. A. T. Turer, J. A. Hill, Pathogenesis of myocardial ischemia-reperfusion injury and rationale for therapy. *Am. J. Cardiol.* **106**, 360–368 (2010).
41. M. L. Lindsey, R. Bolli, J. M. Canty Jr., X.-J. Du, N. G. Frangogiannis, S. Frantz, R. G. Gourdie, J. W. Holmes, S. P. Jones, R. A. Kloner, D. J. Lefer, R. Liao, E. Murphy, P. Ping, K. Przyklenk, F. A. Recchia, L. Schwartz Longacre, C. M. Ripplinger, J. E. Van Eyk, G. Heusch, Guidelines for experimental models of myocardial ischemia and infarction. *Am. J. Physiol. Heart Circ. Physiol.* **314**, H812–H838 (2018).
42. N. Milani-Nejad, P. M. Janssen, Small and large animal models in cardiac contraction research: Advantages and disadvantages. *Pharmacol. Ther.* **141**, 235–249 (2014).
43. Z. Xu, J. Alloush, E. Beck, N. Weisleder, A murine model of myocardial ischemia-reperfusion injury through ligation of the left anterior descending artery. *J. Vis. Exp.* **2014**, e51329 (2014).
44. T. Chen, G. Vunjak-Novakovic, In vitro models of ischemia-reperfusion injury. *Regen. Eng. Transl. Med.* **4**, 142–153 (2018).
45. J. Liao, W. Huang, G. Liu, Animal models of coronary heart disease. *J. Biomed. Res.* **31**, 3–10 (2015).
46. J. J. Chong, C. E. Murry, Cardiac regeneration using pluripotent stem cells—Progression to large animal models. *Stem Cell Res.* **13**, 654–665 (2014).
47. S. Lehoux, A. Tedgui, Cellular mechanics and gene expression in blood vessels. *J. Biomech.* **36**, 631–643 (2003).
48. H. Cui, W. Zhu, Y. Huang, C. Liu, Z.-X. Yu, M. Nowicki, S. Miao, Y. Cheng, X. Zhou, S.-J. Lee, Y. Zhou, S. Wang, M. Mohiuddin, K. Horvath, L. G. Zhang, In vitro and in vivo evaluation of 3D bioprinted small-diameter vasculature with smooth muscle and endothelium. *Biofabrication* **12**, 015004 (2019).
49. J. M. Brazill, Y. Zhu, C. Li, R. G. Zhai, Quantitative cell biology of neurodegeneration in *Drosophila* through unbiased analysis of fluorescently tagged proteins using imageJ. *J. Vis. Exp.* **2018**, e58041 (2018).

Acknowledgments: We would like to thank J. Zou and Y. Lin (IPSC core, NHLBI) for providing hiPSC-CMs and S. Anderson (Animal MRI core, NHLBI) for carrying out the MRI analysis. **Funding:** We also thank American Heart Association Transformative Project Award, NSF EBMS program grant #1856321, and NIH Director's New Innovator Award 1DP2EB020549-01 for financial support. **Author contributions:** H.C., C.L., Y.H., and L.G.Z. conceived the ideas and designed the experiments. H.C., X.Z., and S.-j.L. conducted the in vitro experiments. H.C., Y.H., C.L., Z.-x.Y., and H.S. carried out animal experiments. H.C., C.L., T.E., Y.H., Z.-x.Y., S.Y.H., M.B., M.M., J.P.F., and L.G.Z. performed data analysis and prepared the manuscript. **Competing interests:** A patent application describing the approach presented here was filed by H.C., L.G.Z., and Y.H. (US 62/571,684; PCT/US20 18/055707). The authors declare that they have no other competing interests. **Data and materials availability:** All data needed to evaluate the conclusions in the paper are present in the paper and/or the Supplementary Materials. Additional information related to this paper may be requested from the authors.

Submitted 28 February 2020
Accepted 11 May 2020
Published 24 June 2020
10.1126/sciadv.abb5067

Citation: H. Cui, C. Liu, T. Esworthy, Y. Huang, Z.-x. Yu, X. Zhou, H. San, S.-j. Lee, S. Y. Hann, M. Boehm, M. Mohiuddin, J. P. Fisher, L. G. Zhang, 4D physiologically adaptable cardiac patch: A 4-month in vivo study for the treatment of myocardial infarction. *Sci. Adv.* **6**, eabb5067 (2020).

Science Advances

4D physiologically adaptable cardiac patch: A 4-month in vivo study for the treatment of myocardial infarction

Haitao Cui, Chengyu Liu, Timothy Esworthy, Yimin Huang, Zu-xi Yu, Xuan Zhou, Hong San, Se-jun Lee, Sung Yun Hann, Manfred Boehm, Muhammad Mohiuddin, John P. Fisher and Lijie Grace Zhang

Sci Adv **6** (26), eabb5067.
DOI: 10.1126/sciadv.abb5067

Science Advances (ISSN 2375-2548) is published by the American Association for the Advancement of Science, 1200 New York Avenue NW, Washington, DC 20005. The title *Science Advances* is a registered trademark of AAAS.